ACC Meanders, Energy Transfer, and Mixed Barotropic–Baroclinic Instability

MADELEINE K. YOUNGS

Massachusetts Institute of Technology–Woods Hole Oceanographic Institution Joint Program, Cambridge, Massachusetts

ANDREW F. THOMPSON AND AYAH LAZAR

Environmental Science and Engineering, California Institute of Technology, Pasadena, California

KELVIN J. RICHARDS

International Pacific Research Center, University of Hawai'i at Mānoa, Honolulu, Hawaii

(Manuscript received 8 July 2016, in final form 15 March 2017)

ABSTRACT

Along-stream variations in the dynamics of the Antarctic Circumpolar Current (ACC) impact heat and tracer transport, regulate interbasin exchange, and influence closure of the overturning circulation. Topography is primarily responsible for generating deviations from zonal-mean properties, mainly through standing meanders associated with regions of high eddy kinetic energy. Here, an idealized channel model is used to explore the spatial distribution of energy exchange and its relationship to eddy geometry, as characterized by both eddy momentum and eddy buoyancy fluxes. Variations in energy exchange properties occur not only between standing meander and quasi-zonal jet regions, but throughout the meander itself. Both barotropic and baroclinic stability properties, as well as the magnitude of energy exchange terms, undergo abrupt changes along the path of the ACC. These transitions are captured by diagnosing eddy fluxes of energy and by adopting the eddy geometry framework. The latter, typically applied to barotropic stability properties, is applied here in the depth–along-stream plane to include information about both barotropic and baroclinic stability properties of the flow. These simulations reveal that eddy momentum fluxes, and thus barotropic instability, play a leading role in the energy budget within a standing meander. This result suggests that baroclinic instability alone cannot capture the dynamics of ACC standing meanders, a challenge for models where eddy fluxes are parameterized.

1. Introduction

The Antarctic Circumpolar Current (ACC) plays a key role in the ventilation of dense water masses and the closure of the global overturning circulation (e.g., Marshall and Speer 2012). Recent work has highlighted the impact of the ACC's local dynamics on interbasin transport (Jones and Cessi 2016; Thompson et al. 2016) as well as meridional heat and tracer transport (Dufour et al. 2015). Although eddy kinetic energy (EKE) and isopycnal slopes vary along the path of the ACC, zonally averaged isopycnal slopes have, in general, been found to be insensitive to changes in the wind stress in models and observations (Böning et al. 2008; Abernathey et al. 2011). This effect and the relative insensitivity of the ACC's zonal baroclinic transport to an observed increase in wind stress over the ACC between 1958 and 2000 (Marshall 2003), commonly referred to as "eddy saturation" (Hogg et al. 2008, 2015), has highlighted the need to mechanistically understand both the global and local response of the ACC to a modified surface wind stress (see also Downes and Hogg 2013; Bishop et al. 2016). There is evidence that zonally symmetric increases in wind stress are principally balanced by localized changes in bottom form drag, communicated via interfacial form stress (Ward and Hogg 2011; Thompson and Naveira Garabato 2014; Masich et al. 2015).

Intensification of the surface wind stress over the ACC has been linked to an increase in the baroclinicity of the flow and a subsequent release of energy through baroclinic instability, diagnosed from increased EKE calculated from satellite altimetry-derived velocities (Meredith and Hogg 2006; Hogg et al. 2015). Locally,

Corresponding author: Madeleine K. Youngs, myoungs@mit.edu

DOI: 10.1175/JPO-D-16-0160.1

the increase in EKE is dominated by regions immediately downstream of major topographic features; in regions removed from topography, changes are more moderate. These regions may even experience a suppression of EKE (Bischoff and Thompson 2014; Abernathey and Cessi 2014; Bishop et al. 2016). The magnitude of tracer transport is also heterogeneously distributed in the ACC, with modulations set by interactions between the flow and topographic features (Lu and Speer 2010; Ferrari and Nikurashin 2010; Naveira Garabato et al. 2011; Thompson and Sallée 2012; Abernathey and Cessi 2014; Dufour et al. 2015). Most studies have sought to understand this spatial variability in terms of modifications to the flow's baroclinicity (Chapman et al. 2015; Bischoff and Thompson 2014), although interactions with topography also produce significant changes to the flow's barotropic shear. Here we focus on along-stream transitions in the dynamical regimes of an idealized ACC meander, accounting for both eddy buoyancy and momentum fluxes and thus both baroclinic and barotropic instability, respectively.

Our analysis will primarily consider the dynamical properties of the major standing meanders of the ACC. These regions, located downstream of topographic features, share many similarities with atmospheric storm tracks—regions of elevated EKE (Hoskins and Valdes 1990; Hoskins and Hodges 2002; Chang et al. 2002). The shape and life cycle of atmospheric storm tracks have been, in part, linked to the standing components (i.e., standing meanders) and their ability to modify the local baroclinicity of the flow (Kaspi and Schneider 2011, 2013). While baroclinic instability plays a key role in these interactions, in the atmosphere barotropic instabilities also influence standing meanders (Williams et al. 2007; Chang et al. 2002). A defining characteristic of atmospheric storm tracks is a displacement of regions of peak baroclinicity and peak EKE, which also occurs in fully nonlinear ACC-like scenarios (Chapman et al. 2015) and is related to classical studies of linear instability in domains with along-stream variations in the background stratification (Pierrehumbert 1984; Pedlosky 1989). A key difference is that oceanic standing meanders, or storm tracks, have a separation of characteristic length scales between the standing meander and transient eddies (Williams et al. 2007; Chapman et al. 2015), which influence energy transfer properties of the flow.

An example of the interplay between barotropic and baroclinic instabilities is the barotropic governor. This mechanism was first introduced by James and Gray (1986) to explain why atmospheric simulations with the same baroclinicity but larger barotropic shears have smaller eddy kinetic energy. James (1987) presented both linear and nonlinear characteristics associated with the barotropic governor and found that barotropic shear may suppress the growth of a baroclinically unstable fluid due to the destructive effect of the shear on the exponentially growing normal modes. James (1987) also recognized that the decay of baroclinic eddies may also be responsible for generating or sustaining the barotropic shear. Building on the nonlinear aspect of the barotropic governor, Nakamura (1993) specifically showed that normal-mode baroclinic waves are sensitive to vertically integrated eddy momentum fluxes generated by barotropic shear. The resulting upgradient momentum fluxes limit the conversion of available potential energy into eddy kinetic energy. In other ocean-focused studies, Rivière et al. (2004) found that the baroclinicity often overwhelms the barotropic governor mechanism, but Solodoch et al. (2016) presented Southern Ocean and idealized (respectively) flow regimes with characteristics consistent with the barotropic governor. In this study, by diagnosing both momentum and buoyancy fluxes within and far from the meander, we examine the relevance of this mechanism in the ACC.

Here we adopt the geometric stability method, described in Marshall et al. (2012), Waterman and Hoskins (2013), and Waterman and Lilly (2015), to examine the stability properties and energy conversion rates of an ACC meander with a higher degree of granularity than in earlier studies that have focused primarily on differences between meander and quasi-zonal regions of the ACC. Waterman and Hoskins (2013) showed how the statistics of eddy geometry, calculated for an idealized barotropic jet, agree with simple predictions of eddy–mean energy exchange. More recently, Waterman and Lilly (2015) used the same model to consider the geometric decomposition of eddy feedbacks and showed that both the angle and the anisotropy of transient eddies are important for the evolution of the mean flow. Recently, Tamarin et al. (2016) extended this horizontal analysis to show the consistency of ray-tracing theory with the geometric method. This method is useful for its physical interpretation and connection to linear stability theory. A motivation for this approach is that the horizontal eddy shape can be observed remotely, leading to an assessment of eddy momentum fluxes without the need to compute correlations (Marshall et al. 2012). A global analysis in this framework was carried out by Stewart et al. (2015) using a global general circulation model. These previous studies [with the exception of Marshall et al. (2012)] only consider barotropic flow regimes, and therefore the statistical description of the eddy geometry is limited to the horizontal plane. The ACC, however, has a significant baroclinic component, which motivates our adoption of the generalized

three-dimensional eddy geometry developed by Marshall et al. (2012).

Using an idealized MITgcm channel model with a meridional ridge, we examine the three-dimensional shape of transient eddies to determine their evolution and interaction with ACC meanders; these diagnostics are compared with energy conversion terms. Diagnosing both kinetic and potential energy conversions allows us to assess the relative importance of both barotropic and baroclinic instabilities in the life cycle of an ACC meander. The model and methods are described in section 2. In section 3, we discuss the spatial distribution of energy conversion terms and analyze the localization of this exchange. Following Marshall et al. (2012), we examine the geometric stability of the domain in section 4. In section 5, these results are interpreted in terms of the interaction between barotropic and baroclinic instabilities and are compared to previous studies of storm tracks and jet regions; we conclude with a summary in section 6.

2. Methods

a. Energy conversion

We begin our analysis of the meander system by considering both the kinetic and potential energy budgets. We focus on those terms that describe the exchange of energy between mean and eddy energy reservoirs. We define the mean kinetic energy (MKE) of the flow as

$$\mathrm{MKE}(x,y,z) = 0.5\rho_0(\overline{u}^2 + \overline{v}^2), \tag{1}$$

and the EKE as

$$\mathrm{EKE}(x,y,z) = 0.5\rho_0\overline{(u'^2 + v'^2)}, \tag{2}$$

where u is the zonal velocity, v is the meridional velocity, ρ_0 is a constant reference density, overbars denote a time average (in our simulations a period of 13 years), and primes denote deviations from the time mean. For the potential energy, we adopt the quasigeostrophic framework. This implies an assumption that perturbations to the stratification are small compared to the mean stratification. This could appropriately be questioned across the standing meander and downstream regions, but we adopt this assumption for tractability and note that the quasigeostrophic framework has been shown to often apply outside its formal limits (Williams et al. 2010). The mean available potential energy (MAPE) is given by

$$\mathrm{MAPE}(x,y,z) = \frac{0.5}{\mathscr{N}_0^2(z)\rho_0}\overline{\rho^*(x,y,z,t)}^2, \tag{3}$$

and the eddy available potential energy (EAPE) is given by

$$\mathrm{EAPE}(x,y,z) = \frac{0.5}{\mathscr{N}_0^2(z)\rho_0}\overline{\rho'(x,y,z,t)^2}, \tag{4}$$

where $\mathscr{N}_0^2(z)$ is the squared buoyancy frequency computed from a domain-averaged, time-mean density profile, $\rho^*(x,y,z,t) = \rho(x,y,z,t) - \overline{\langle\rho(x,y,z,t)\rangle}$, and $\rho'(x,y,z,t) = \rho(x,y,z,t) - \overline{\rho(x,y,z,t)}$, where $\langle\cdot\rangle$ indicate a domain average at a given depth. From these definitions, governing equations for kinetic and potential energy may be derived as in Chen et al. (2014); interactions between eddies and the mean flow give rise to exchange between these energy reservoirs. This framework also isolates the baroclinic and barotropic instability pathways, which allows comparison to the geometric method, outlined in section 2b.

We consider the following five terms in this study following Chen et al. (2014):

- the rate of change of MAPE from horizontal eddy density (buoyancy) fluxes (D_{P_M}):

$$D_{P_M} = -\frac{\overline{\rho^*}}{\mathscr{N}_0^2(z)\rho_0}\nabla_H\cdot\overline{(\mathbf{u}_H'\rho')}, \tag{5}$$

  where $\mathbf{u}_H$ is the horizontal velocity vector and ∇_H is the horizontal gradient operator;
- the rate of change of eddy energy (EKE and EAPE) due to horizontal eddy density (buoyancy) fluxes (D_{P_E}):

$$D_{P_E} = -\frac{1}{\mathscr{N}_0^2(z)\rho_0}\overline{(\mathbf{u}_H'\rho')}\cdot\nabla_H\overline{\rho^*}; \tag{6}$$

- the rate of change in EKE from EAPE (D_{K_E}):

$$D_{K_E} = -g\overline{\rho'w'}, \tag{7}$$

  where w is the vertical velocity and g is the gravitational acceleration constant;
- the rate of change in MKE due to eddy momentum fluxes (M_{K_M}):

$$M_{K_M} = -\rho_0[\overline{u}\nabla\cdot\overline{(u'\mathbf{u}')} + \overline{v}\nabla\cdot\overline{(v'\mathbf{u}')}]; \tag{8}$$

- and the rate of change of EKE due to eddy momentum fluxes (M_{K_E}):

$$M_{K_E} = -\rho_0(\overline{u'\mathbf{u}'}\cdot\nabla\overline{u} + \overline{v'\mathbf{u}'}\cdot\nabla\overline{v}). \tag{9}$$

The baroclinic instability pathway is described by the D terms D_{P_M}, D_{P_E}, and D_{K_E}, as they represent the flow of energy from MAPE to EAPE to EKE due to eddies. Barotropic instability is represented by the M terms M_{K_M} and M_{K_E} because these terms represent the extraction of MKE due to eddies and the growth of

EKE, respectively. Terms D_{P_M} and D_{P_E} are related but not identical: integrating D_{P_M} by parts results in D_{P_E} as well as an additional term that integrates to zero over the domain but does not disappear locally (the same is true when the two terms are swapped). The additional term here contains the energy advection and other residual terms. The relationship between M_{K_M} and M_{K_E} is analogous. The other terms in the energy equations, such as dissipation, are not pertinent for our stability analysis and are not discussed. See Chen et al. (2014) for further information about these terms.

We note that D_{P_E} contains both the rotational and divergent components of the buoyancy fluxes. The rotational component, which is customarily removed, corresponds to the growth and decay of eddies in the domain (Marshall and Shutts 1981). Since we are interested in the eddy life cycles, we choose to use the full fluxes.

b. Eddy geometry

In addition to the energy conversion terms described above, we also employ an eddy shape analysis to examine eddy–mean flow interactions within the meander. While the geometric diagnostics essentially use the same information as the conversion terms—eddy fluxes of momentum and buoyancy—the geometric framework has proven insightful in mapping the spatial distribution of eddy–mean flow interaction (Waterman and Lilly 2015). The derivation of the eddy geometry terms is provided in Marshall et al. (2012).

We define

$$M = \frac{\overline{v'^2 - u'^2}}{2}, \quad N = \overline{u'v'}, \tag{10}$$

which are related to the eddy Reynolds stresses, and

$$R = \frac{f_0 g}{\mathscr{N}_0^2(z)\rho_0}\overline{u'\rho'}, \quad S = \frac{f_0 g}{\mathscr{N}_0^2(z)\rho_0}\overline{v'\rho'}, \tag{11}$$

which are components of eddy buoyancy flux and are proportional to eddy interfacial form stress.

From these terms we define a horizontal anisotropy parameter

$$\gamma_m = \frac{\sqrt{M^2 + N^2}}{\mathrm{EKE}}, \quad 0 \le \gamma_m \le 1, \tag{12}$$

which is the ratio of the eddy Reynolds stresses to the eddy kinetic energy. This measures the eccentricity in the horizontal shape of the eddy, or equivalently the anisotropy in the eddy momentum fluxes. When $\gamma_m \approx 0$ the flow is approximately isotropic; the flow becomes more anisotropic as γ_m approaches 1. A measure of the dominant (or time averaged) angle ϕ_m of the eddy momentum fluxes is given by

$$\phi_m = \frac{1}{2}\cos^{-1}\left(-\frac{M}{\sqrt{M^2 + N^2}}\right), \quad 0 \le \phi_m \le \pi. \tag{13}$$

Here, ϕ_m is the angle of the eddy momentum fluxes with respect to the zonal direction in the horizontal plane (Fig. 1). This decomposition can also be undertaken for the buoyancy fluxes, with

$$\gamma_b = \frac{N(z)}{2f_0}\sqrt{\frac{R^2 + S^2}{\mathrm{EKE} \times \mathrm{EAPE}}}, \quad 0 \le \gamma_b \le 1, \tag{14}$$

which represents the relative magnitude of the eddy buoyancy fluxes to the eddy potential and kinetic energies, or the anisotropy in the eddy buoyancy fluxes. There is also a corresponding angle

$$\phi_b = \cos^{-1}\left(\frac{R}{\sqrt{R^2 + S^2}}\right), \quad -\pi \le \phi_b \le \pi, \tag{15}$$

which gives the dominant direction of the eddy buoyancy fluxes in the horizontal plane. We also define

$$\frac{\mathrm{EAPE}}{\mathrm{EKE}} = \tan^2\lambda, \quad 0 \le \lambda \le \pi/2, \tag{16}$$

where λ measures the partitioning of total eddy energy into kinetic and potential components, or the baroclinicity of the flow. We then project the eddy buoyancy fluxes into the vertical–along-stream plane to describe the eddy fluxes for baroclinic eddies similar to the horizontal interpretation used for barotropic eddies. We take

$$\tan 2\phi_t = \gamma_b \tan 2\lambda, \quad \gamma_t = \frac{\cos 2\lambda}{\cos 2\phi_t}, \quad 0 \le \gamma_t \le 1, \tag{17}$$

where ϕ_t is the angle in the x–z plane with respect to the horizontal plane and γ_t is a measure of the eccentricity of the eddy fluxes in the vertical direction (Fig. 1). Since the channel flow is not purely zonal, we project ϕ_t onto the plane that is perpendicular to the direction of ϕ_b, giving the sign of the eddy buoyancy fluxes. These diagnostics provide the stability and anisotropy parameters for baroclinic instability, which is related to the magnitude and direction of the eddy buoyancy fluxes (Marshall et al. 2012).

Larger anisotropy—given by γ_m in the horizontal and γ_t in the vertical—of the eddy fluxes is associated with stronger eddy–mean flow interactions. The angle of the eddy (ϕ_m, ϕ_t), with respect to the mean flow determines the stability of the flow, is represented schematically in Fig. 1. When the eddy, represented by

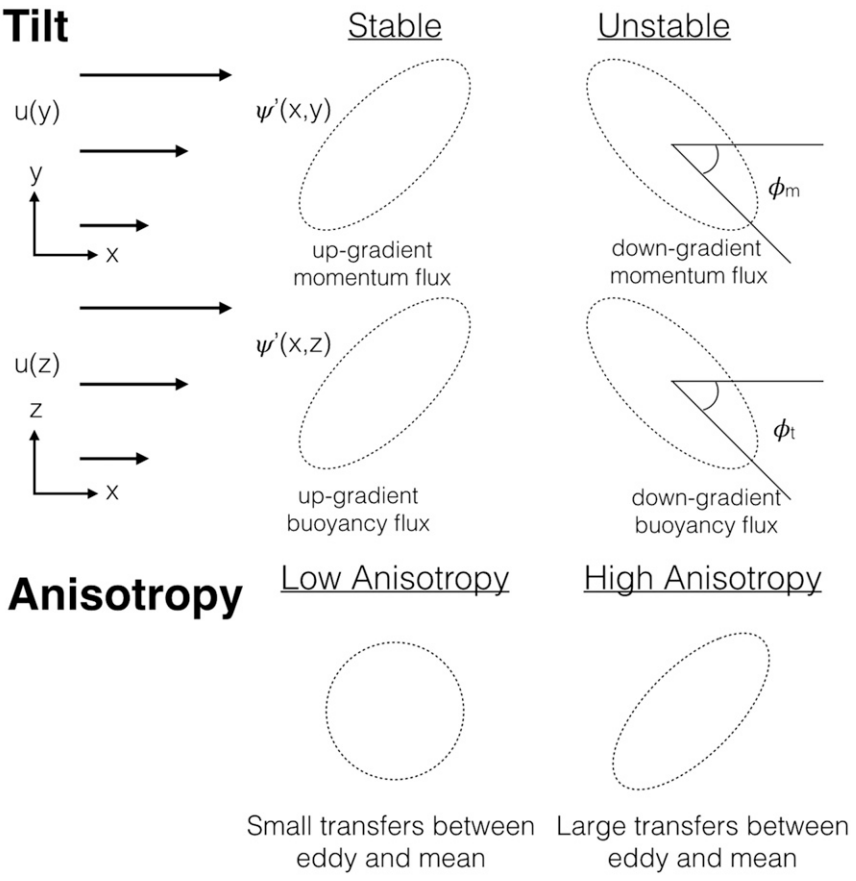

FIG. 1. Schematic relating eddy orientation and stability [both (top) barotropic and (middle) baroclinic] and (bottom) relating anisotropy and energy transfer. The black arrows to the left show the shear related to the mean flow u, and the dashed lines are the eddy streamfunction contours ψ'. Purely barotropic eddies tilt in the horizontal (top) and ψ' is a function of u' and v'; purely baroclinic eddies tilt in the vertical (middle) and ψ' is a function of v' and b'. When the eddy major axis tilts with the shear, the eddies are stable and decay, giving energy to the mean flow, which increases the shear. When the eddy major axis tilts against the shear, the eddies are unstable and grow, taking energy from the mean flow, which reduces the shear.

an eddy streamfunction, tilts against the mean flow shear, the perturbation is growing and extracting energy from the mean flow. When the eddy is tilted with the mean flow shear, the perturbation is decaying and exchanging energy back into the mean flow (Pedlosky 2013). For energy to transfer between the mean and eddy components, the eddy flux anisotropy and eddy streamfunction tilt must both be nonzero, with larger anisotropy, $\gamma \to 1$, providing more effective energy transfer. This conceptual picture has been effective in describing barotropic flows (Waterman and Lilly 2015) and can be extended to describe the physical shape of a barotropic eddy. The physical interpretation is more challenging when extended to the vertical because the eddy geometry now depends on eddy buoyancy fluxes instead of just eddy momentum fluxes, that is, depends on u', v', and b'. Nevertheless, below we show that the eddy orientation provides a consistent picture when compared to the more traditional energy conversion terms.

c. Model

The goal of our model configuration is to resolve mesoscale eddy dynamics in a reentrant channel of a sufficient length that will allow us to analyze the alongstream structure of the eddy–mean flow interactions in three different regimes: upstream, within, and downstream of the meander. Our experiment is designed to have a negligible residual overturning circulation as there is no surface buoyancy forcing and weak interior diapycnal mixing. Thus, the eddy overturning completely balances the wind-induced circulation. We use the MITgcm (Marshall et al. 1997) in the Boussinesq and hydrostatic approximations on a β plane [$f(y) = -10^{-4} + 10^{-11}y$] with a Cartesian grid

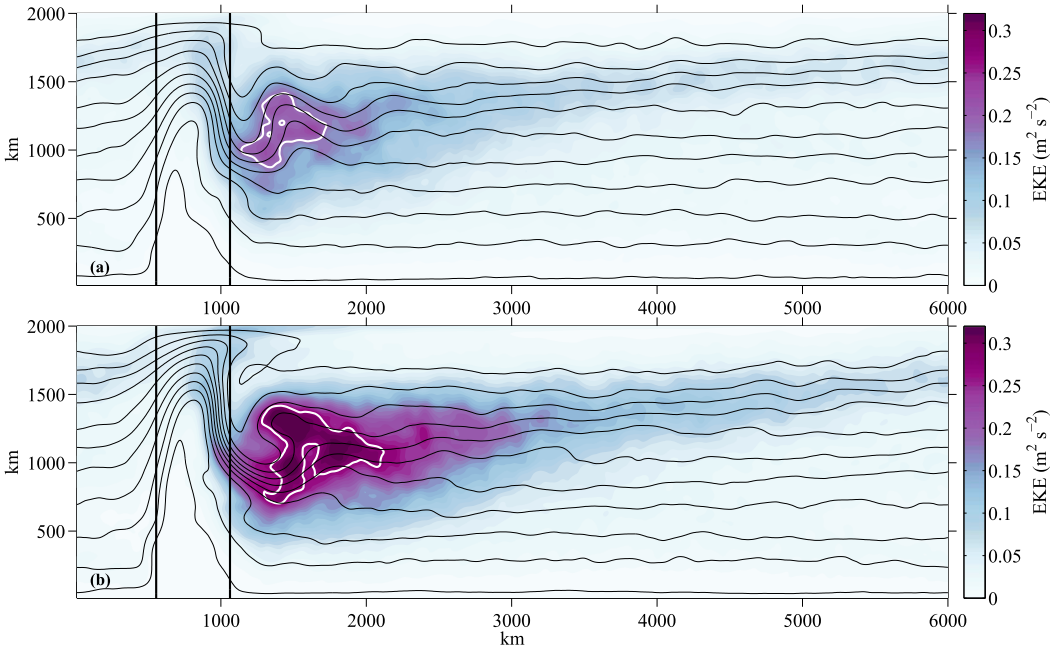

FIG. 2. Eddy kinetic energy at 177-m depth for experiments with wind stress forcing (a) $\tau_0 = 0.1\,\mathrm{N\,m^{-2}}$ and (b) $\tau = 0.2\,\mathrm{N\,m^{-2}}$. Thick white contours indicate the region containing EKE that is at least 80% of the peak EKE. Thin lines show potential temperature contours and are separated by 1°C. Thick lines show where the Gaussian ridge, centered at 800 km, rises above 3800-m depth.

where x is the zonal coordinate and y is the meridional coordinate. The domain is 6000 km long (zonal), 2000 km wide (meridional), and 4000 m deep (vertical). We add topography in the form of a simple cross-channel Gaussian ridge centered at $x = x_0$:

$$h_b(x) = -H + h_0 e^{-(x-x_0)^2/\sigma^2},$$

where $h_0 = 1000\,\mathrm{m}$, $\sigma = 200\,\mathrm{km}$, and $x_0 = 800\,\mathrm{km}$ (Fig. 2). The blocking ridge allows the momentum input by the wind to be dissipated by bottom form drag. The deformation radius is approximately 35 km and the grid spacing is 10 km, so that the model is eddy resolving. There are 32 vertical levels increasing from 50 m at the surface to 200 m at depth. Linear bottom drag with a drag coefficient of $1.1 \times 10^{-3}\,\mathrm{m\,s^{-1}}$ is applied, and we impose free slip boundary conditions at the north and south boundaries. The density is prescribed by a linear equation of state with temperature only; the reference density is $\rho_0 = 1000\,\mathrm{kg\,m^{-3}}$ and the thermal expansion coefficient is $\alpha = 2 \times 10^{-4}\mathrm{°C^{-1}}$. The model horizontal explicit diffusivity is set to zero and the vertical diffusivity is $5 \times 10^{-6}\,\mathrm{m^2\,s^{-1}}$, which is comparable to the effective numerical diffusivity, meaning the interior is almost completely adiabatic. Subgrid processes are represented by a horizontal eddy viscosity of $12\,\mathrm{m^2\,s^{-1}}$ and a vertical viscosity of $3 \times 10^{-4}\,\mathrm{m^2\,s^{-1}}$. The temperature at the northern boundary is relaxed to an exponential profile from 20°C at the surface to 0°C at depth:

$$\theta(z) = 20(e^{z/1000} - e^{-H/1000})/(1 - e^{-H/1000}),$$

with a relaxation period of 1 week. This relaxation is applied linearly over a meridional extent of 100 km. We apply a zonal wind stress, $\tau^x(y) = \tau_0 \sin(\pi y/L_y)$, with two different maxima, $\tau_0 = 0.1$ and $0.2\,\mathrm{N\,m^{-2}}$, and no surface buoyancy forcing. We use yearly averages of 13 model years after an equilibration period of 27 years for both wind stresses. Examples of the model output are shown in Fig. 2. The depth and spatially averaged zonal velocity is $4\,\mathrm{cm\,s^{-1}}$ for $\tau_0 = 0.1\,\mathrm{N\,m^{-2}}$ and $4.4\,\mathrm{cm\,s^{-1}}$ for $\tau_0 = 0.2\,\mathrm{N\,m^{-2}}$. The spatially averaged surface zonal velocities are $13\,\mathrm{cm\,s^{-1}}$ for $\tau_0 = 0.1\,\mathrm{N\,m^{-2}}$ and $13.4\,\mathrm{cm\,s^{-1}}$ for $\tau_0 = 0.2\,\mathrm{N\,m^{-2}}$. Mean surface velocities of the ACC are around $20\,\mathrm{cm\,s^{-1}}$ (Talley 2011).

3. Energy conversion

We first present the energy conversion terms to diagnose the spatial patterns of the eddy–mean flow interactions. The diagnosed depth-averaged eddy energy conversion terms are defined in section 2a. The largest amplitudes of D_{P_M} [(5)] are negative, indicating a loss of

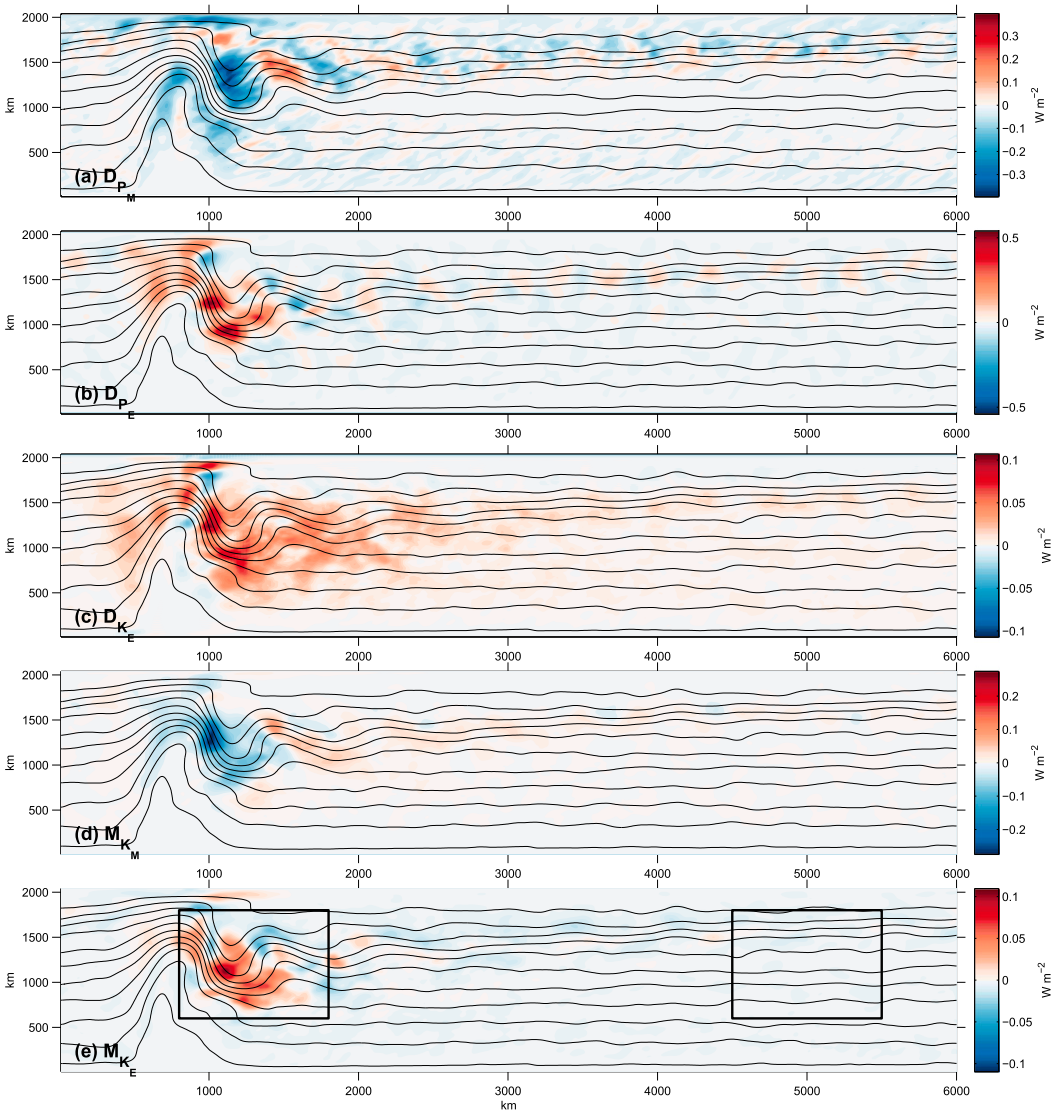

FIG. 3. Depth-integrated energy conversion terms (W m^{-2}) for the experiment with $\tau_0 = 0.1$ N m^{-2}. Contour lines show temperature every degree Celsius at 177-m depth. Term D_{P_M} is the rate of change of MAPE due to horizontal eddy fluxes [(5)], D_{P_E} is the rate of change of eddy energy due to horizontal eddy density fluxes [(6)], D_{K_E} is the rate of change in EKE from EAPE [(7)], M_{K_M} is the rate of change in MKE due to eddy momentum fluxes [(8)], and M_{K_E} is the rate of change in EKE due to eddy momentum fluxes [(9)].

MAPE and occur on the flanks of the jet, whereas the largest amplitudes of D_{P_E} [(6)] are positive, indicating a gain of EAPE and occur within the core of the jet (Figs. 3, 4). This implies that the eddy–mean flow interactions are spatially nonlocal. Both D_{P_M} and D_{P_E} are largest in the lee of ridge, but are peaked upstream of the region where EKE is largest (Fig. 2).

In contrast, the patterns of D_{P_E} and D_{K_E} are quite similar and have the same sign. This is consistent with the baroclinic instability pathway, highlighting regions where EAPE is converted into EKE. The magnitude of D_{K_E} [(7)] is smaller than D_{P_E}, suggesting that not all of the EAPE is transformed into EKE in these locations. This difference results from a combination of a flux of EAPE out of the domain, as well as dissipation, and potentially conversion into MKE (Chen et al. 2016).

The conversion of MKE from the eddy momentum fluxes, M_{K_M} [(8)], is peaked at the same location as the MKE field (not shown), within the core of the jet, and is a sink of MKE. Term M_{K_E} [(9)] has its largest amplitude further downstream along the flanks of the jet and coincides with the region of largest horizontal shear. Here the Reynolds stresses are most efficient at extracting energy from the mean flow, resulting in

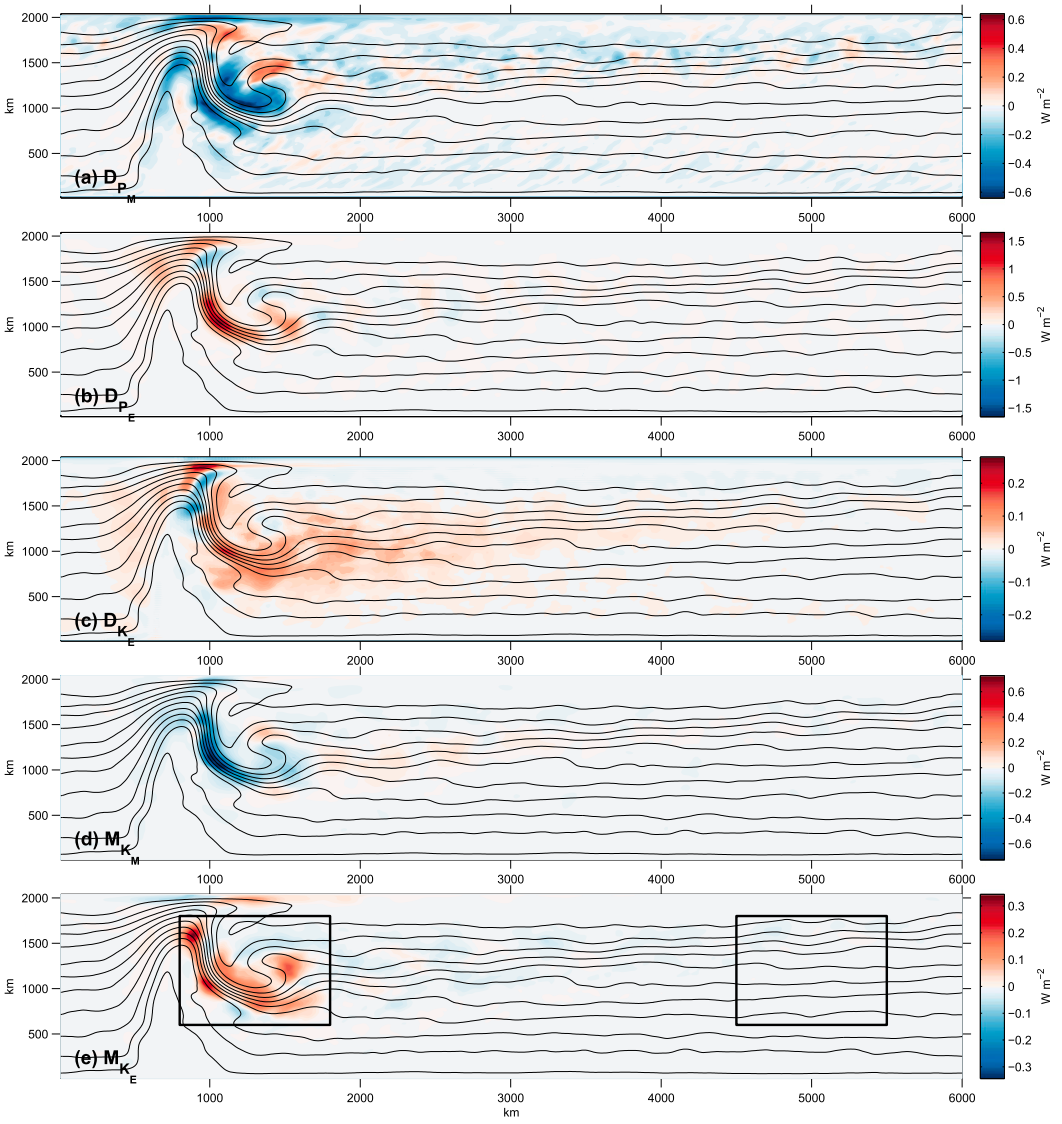

FIG. 4. As in Fig. 3, but depth-integrated energy conversion terms (W m^{-2}) with $\tau_0 = 0.2$ N m^{-2}.

barotropic instability. Overall, the conversion from EAPE (D_{K_E}) and from MKE (M_{K_E}) into EKE have the same magnitudes in the meander region both peaking around 0.1 W m^{-2}, consistent with a mixed instability process.

Comparing the two imposed wind stress amplitudes, all conversion terms have larger magnitudes for the $\tau_0 = 0.2$ N m^{-2} experiment (Figs. 3, 4). This is consistent with a mechanically induced increase in the EAPE reservoir; the stronger wind stress generates a larger-amplitude, near-surface Ekman convergence and divergence. However, qualitatively there is no appreciable change in the physical extent of the conversion region with a change in winds, which differs from the results of Bischoff and Thompson (2014). In this previous study, which used a Gaussian bump instead of a ridge, the physical extent of the storm track was strongly sensitive to the magnitude of the wind stress.

The relative insensitivity of the zonal baroclinic mean flow to the wind stress is a common feature of these ACC-like channel models, a property known as eddy saturation, but the sensitivity of the energy budget and the exchange between different reservoirs has been explored to a lesser extent. We consider the regionally averaged energy characteristics using a Lorenz diagram similar to those used in Chen et al. (2014) (Fig. 5). Within the meander, defined by boxes on the left-hand side of Figs. 3 and 4, eddy fluxes consistent with barotropic instability are a primary component of energy transfer. This is represented by the conversion of MKE

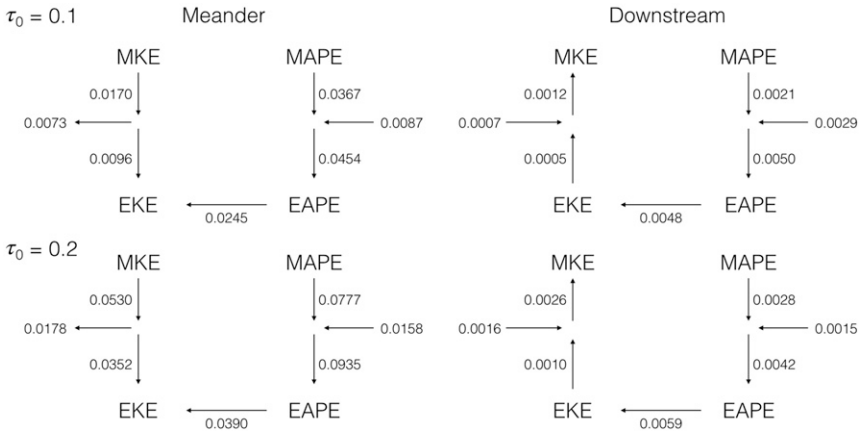

FIG. 5. Lorenz diagram from two different regions, indicated by the boxes in Figs. 3 and 4. The meander region is located just downstream of the ridge and the downstream domain refers to a region with quasi-zonal jets. The values provided in the diagram are depth-integrated, domain-averaged quantities (W m^{-2}). The diagrams follow those shown in Chen et al. (2014).

into EKE, which occurs in a barotropically unstable system. In contrast, downstream of the meander, defined by the right-hand boxes in Figs. 3 and 4, EKE is converted back to MKE, consistent with upgradient eddy momentum fluxes. In the downstream domain, there is an excess of energy being introduced from upstream, consistent with advection out of the upstream domain shown in the Lorenz diagram.

For the potential energy transfer components of the Lorenz diagram, in both regions, MAPE is converted into EAPE, which is then converted into EKE: the traditional baroclinic instability energy pathway. However, D_{P_E} is larger than D_{P_M}, so EAPE enters each domain through a different process. This "leak" in the system could be advection downstream, a delay phenomenon discussed in Chen et al. (2016), the propagation of energy downstream at the group velocity (Chapman et al. 2015), or another process. This suggests that eddy potential energy may be transported downstream where there is sufficient time to complete the conversion to EKE. This is supported by the displacement between regions of enhanced baroclinicity and the maximum in EKE (Bischoff and Thompson 2014; Chapman et al. 2015).

With a change in wind stress, the magnitude of the energy transfers in the Lorenz diagram tends to increase. Within the meander, the conversion of MAPE to EAPE is doubled when the wind stress is doubled, but the conversion of EAPE to EKE is only increased by 60%. The conversion of MKE to EKE, on the other hand, increases by over 3.5 times. We see that as the wind stress increases, the total contribution to EKE changes from mostly from EAPE to almost the exact same magnitude between EAPE and MKE. In the downstream region, the conversion of EKE to MKE is doubled when the wind stress is doubled, but the conversion between MAPE to EKE is basically unchanged.

To summarize, in the meander regions, the fluxes of EAPE to EKE and of MKE to EKE are both downgradient and roughly the same magnitude, consistent with mixed instability. In the downstream region, the buoyancy fluxes are downgradient, consistent with baroclinic instability, but the momentum fluxes are upgradient. However, in this region the energy leaving EKE due to eddy momentum fluxes (M_{K_E}) is significantly smaller than the energy entering EKE though the baroclinic pathway (D_{K_E}). These upgradient momentum fluxes could result from several phenomena, including eddies that have been generated elsewhere, advected into a region, and subsequently sheared by the mean flow or through baroclinic instability (Pedlosky 2013).

4. Geometric analysis

Analyzing the same simulations using the geometric framework described in section 2b produces a similar interpretation of the instability and energy conversion properties of the flow. However, this geometric method can provide a more physical interpretation of the energy exchange terms. The angles of the eddies with respect to the mean flow have a direct analogy to linear stability theory (Marshall et al. 2012; Pedlosky 2013). When the eddies are tilted with the shear, they are giving energy to the mean flow, corresponding to stability, and when the eddies are tilted against the shear, they are growing and taking energy from the mean flow, corresponding to instability (Fig. 1).

For our geometric analysis we first analyze the flow in the horizontal, 2D plane, similar to Waterman and Lilly

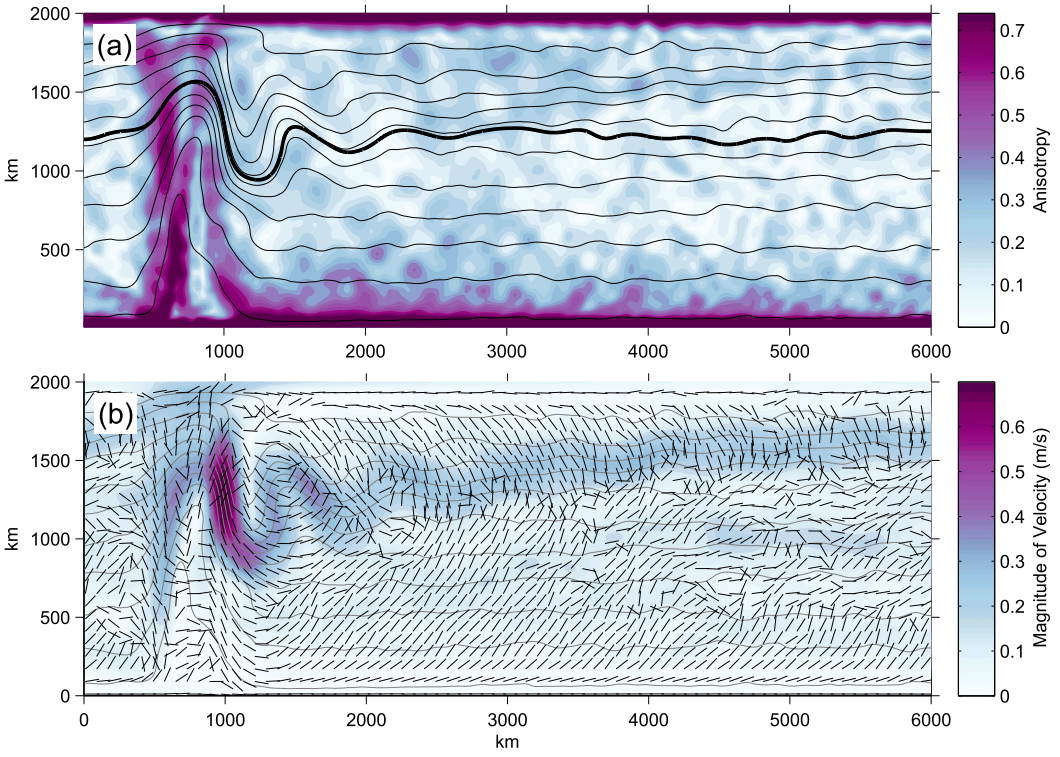

FIG. 6. (a) Depth-averaged eddy anisotropy in color and (b) the tilt for $\tau_0 = 0.1\,\mathrm{N\,m^{-2}}$; both diagnostics are dimensionless. The color shows the magnitude of the velocity at 177-m depth. The temperature is contoured every degree at 177-m depth, and the bold line is a streamline computed from the velocities and is used in Fig. 8.

(2015). Using depth-averaged (i.e., vertical average weighted by the layer thickness) anisotropy, we find that topography locally modifies eddy anisotropy (Figs. 6, 7). In the case where $\tau_0 = 0.2\,\mathrm{N\,m^{-2}}$, elevated anisotropy occurs on the flanks of the jet as the meander deflects southward. This highlights a key role for the topography: in order to conserve potential vorticity and mass, streamlines tighten upon crossing the ridge, which increases the horizontal shear and the potential for barotropic instability. We also speculate that rapid changes in the orientation of the streamlines can produce regions where coherent eddies are transiently tilted against the mean shear before adjusting to the new shear orientation—a form of eddy memory related to the finite adjustment time of a coherent eddy in a spatially variable mean flow. Analysis of the horizontal eddy tilt is complicated because of the changing orientation of the streamlines (as opposed to perfectly horizontal streamlines; Waterman and Lilly 2015). Within the meander itself, though, the momentum fluxes tend to be downgradient, or the eddies are tilted against the mean flow shear. Immediately downstream of the meander at about $x = 1500$ km, where the analysis is easier, all eddies tilt with the shear corresponding to upgradient momentum fluxes. The sign of the momentum fluxes agrees with the distribution of M_{K_E} (Fig. 4d). There are elevated regions of eddy anisotropy near the northern and southern boundaries that are due to geometrical constraints of the numerical simulation, and we do not focus on these regions (Figs. 6, 7).

Next we consider the vertical eddy geometry (3D flow), which provides information about the interactions between baroclinic eddies and the mean flow. The vertical anisotropy is high in several locations, particularly over the ridge and downstream of the ridge. There are sporadic instances of high vertical anisotropy in the remainder of the domain as well (Figs. 8, 9). In the downstream, quasi-zonal jet region, the rapid changes of the eddy anisotropy are partly related to an imperfect agreement between the jet cores and the streamline used for the along-stream analysis. The flow generally has downgradient buoyancy fluxes over and around the ridge. The one exception is that for the $\tau_0 = 0.2\,\mathrm{N\,m^{-2}}$ case, just downstream of the ridge, the flow has both low anisotropy and upgradient buoyancy fluxes in a small region.

A comparison of the spatial characteristics of the vertical eddy geometry in Figs. 8 and 9 are also largely consistent with the D_{P_E} (conversion to EAPE from MAPE) patterns in Figs. 3b and 4b. For instance, for $\tau_0 = 0.2\,\mathrm{N\,m^{-2}}$, the flow has upgradient buoyancy fluxes before the maximum shear, as indicated by the vertical

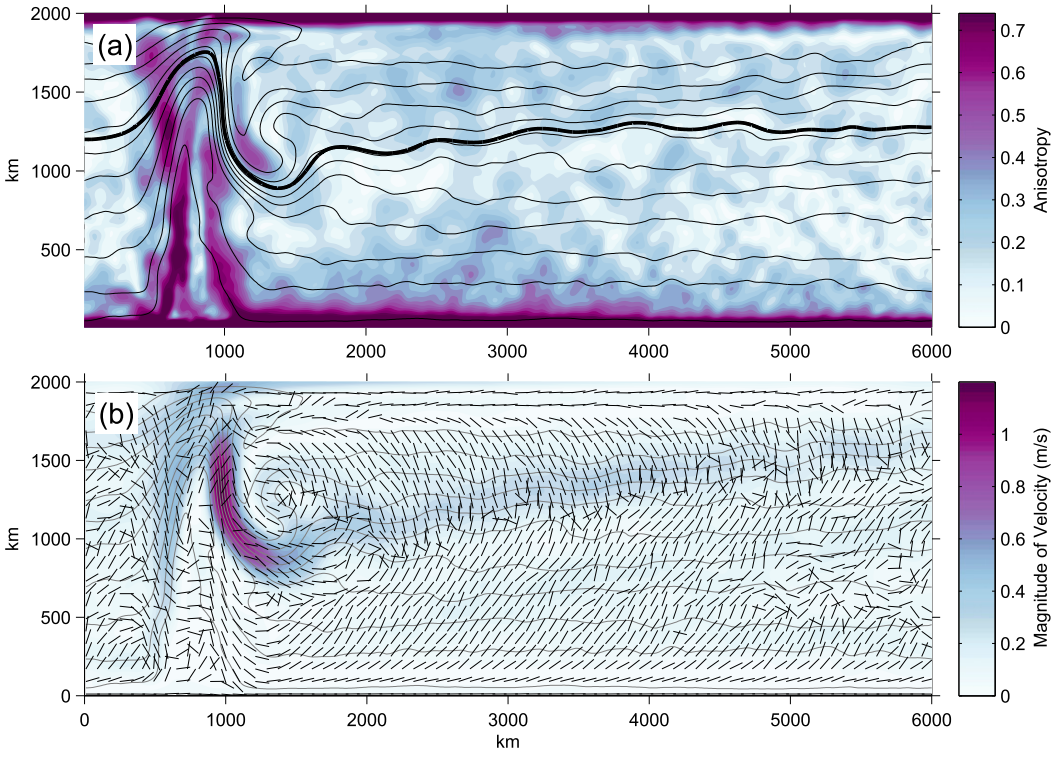

FIG. 7. (a) Depth-averaged eddy anisotropy in color and (b) the tilt for $\tau_0 = 0.2\,\mathrm{N\,m^{-2}}$; both diagnostics are dimensionless. The color shows the magnitude of the velocity at 177-m depth. The temperature is contoured every degree at 177-m depth and the bold line is a streamline computed from the velocities and is used in Fig. 9.

anisotropy combined with the vertical tilt. Downstream of the maximum shear, the flow has downgradient buoyancy fluxes, as indicated by the large conversions into EAPE (D_{P_E}), and the high vertical anisotropy and unstable tilt in the vertical. When $\tau_0 = 0.1\,\mathrm{N\,m^{-2}}$, the flow has downgradient buoyancy fluxes, which is again consistent with the eddy vertical tilt and anisotropy. Eddy buoyancy fluxes are more consistently downgradient throughout the domain, as compared to the eddy momentum fluxes, but the amplitude of the buoyancy fluxes and momentum fluxes become similar in the meander region leading to mixed instability.

5. Discussion

a. Mixed instability in the ACC

The large-scale tilt of density surfaces across the ACC highlights the importance of baroclinic instability in setting the current's equilibrated structure. A close analysis of eddy energy transfers in the most energetic regions of the ACC, the major standing meanders, suggests that baroclinic conversion alone is insufficient to describe both the stratification and distribution of EKE. The magnitude of energy transfer into EKE via M_{K_E} and D_{K_E}, the barotropic and baroclinic pathways in the meander, respectively, are approximately the same (Figs. 3–5). This reflects the reduction in spatial scale of the core of the ACC, which magnifies the horizontal shear until barotropic instability becomes important (Killworth 1980). The flow is then in a regime of mixed instability. With a change in the magnitude of the wind stress, we see a difference in the shape of the meander, with a narrower jet for the case where $\tau_0 = 0.2\,\mathrm{N\,m^{-2}}$, which would imply a larger contribution of barotropic instability, a hypothesis that is verified by energy conversion terms (Fig. 5). Thus, changes in wind stress could change the relative importance of barotropic and baroclinic instabilities in this system. This more complicated view of baroclinic instability is potentially a problem for model parameterizations because they do not take background shear into account, which could result in an incorrect partitioning of energy.

The notion that barotropic instability may play a leading-order role in the equilibration of standing meanders and therefore impact larger-scale properties of the ACC has received little attention. Indeed, Vallis (2006, chapter 16.6) uses a scaling analysis to suggest that the lateral momentum fluxes can be neglected in comparison to the eddy buoyancy fluxes. However, this is based on bulk properties of the ACC, which are modified significantly

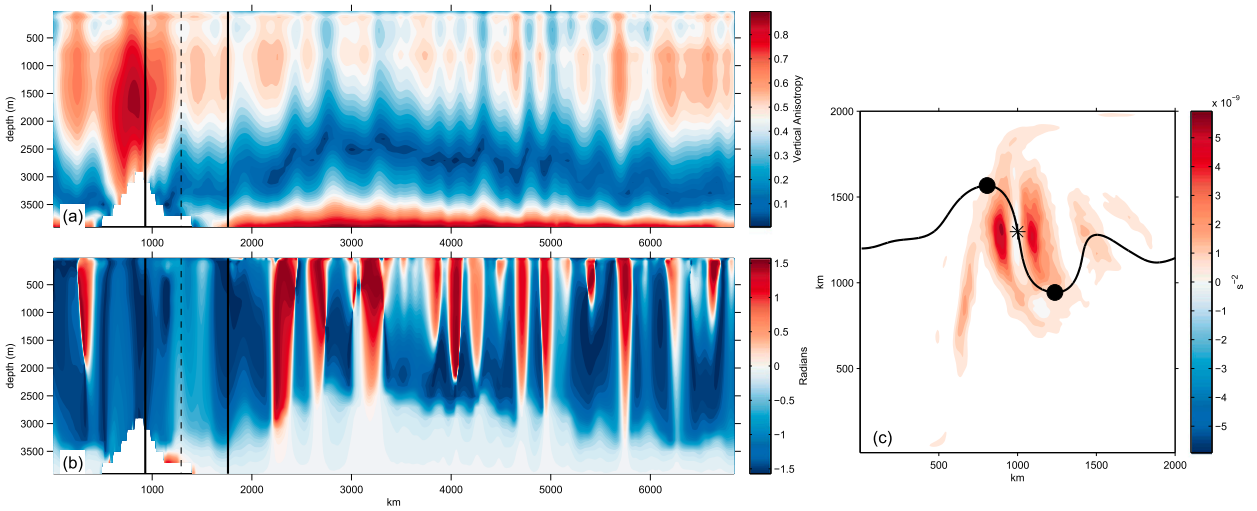

FIG. 8. (a) Vertical eddy anisotropy and (b) the tilt into the vertical with respect to the mean flow [(16)] for $\tau_0 = 0.1$ N m^{-2}. The calculations are complete along the streamline shown in Fig. 6. The solid black lines show the location of the black dots in (c) and the dashed line shows the location of the asterisk in (c). A positive tilt (red) represents downgradient buoyancy fluxes, and a negative (blue) tilt represents upgradient buoyancy fluxes. (c) A measure of the horizontal shear $|\nabla u|^2 + |\nabla v|^2$ with the streamline followed in (a) and (b).

within the standing meanders, as described above. The elevation of the eddy momentum fluxes and the importance of barotropic instability in the meander have important implications. The momentum balance is typically described as a balance between input from surface winds and the vertical transfer, via interfacial form stress, to the solid earth. It is baroclinic instability and eddy buoyancy fluxes that carry out this vertical transfer. As eddy momentum fluxes become more important, a larger proportion of this momentum can be diverged laterally or, as shown here, exchanged back to the mean flow and carried away from the regions with significant topographic features. Finally, interfacial form stress is intricately linked to the overturning circulation through the meridional transfer of mass and heat related to the coupled nature of eddy buoyancy, heat, and thickness fluxes (Marshall and Speer 2012). A change in the partitioning of barotropic or baroclinic instability properties in response to a change in surface wind stress will then also impact the overturning circulation.

As discussed in the introduction, the incomplete conversion of EAPE to EKE has, in the atmospheric literature, been associated with the barotropic governor mechanism. It occurs because during the growth process of baroclinic eddies, some of the EAPE may be converted into MKE through upgradient momentum fluxes when there is a barotropic shear. Thompson and Richards (2011) have used model output to suggest that upgradient momentum fluxes might be relevant in the ACC. However, baroclinic growth is not the only mechanism responsible for generating upgradient momentum fluxes. Advection of energy between different regions of the domain or the barotropic decay of eddies could also result in the upgradient momentum flux as well. The energy analysis here indicates that upgradient fluxes of momentum are collocated with downgradient fluxes of buoyancy. This arrangement is consistent with the description of the barotropic governor provided by Nakamura (1993), where upgradient momentum fluxes occur in a baroclinically unstable flow. The flow has both a barotropic and baroclinic shear, which can interact, leading to mixed instability and feedbacks.

b. *Meander life cycle*

The focus on energy transfer diagnostics across a single meander provides insight into the life cycle of fluid parcels passing through this localized region, offering a more nuanced view of eddy–mean flow interactions in the complex ACC. Upstream of the meander there are upgradient momentum fluxes that remove energy from the eddies and accelerate the mean flow, predominantly in narrow jets with a lateral scale comparable to the deformation radius. The jets are steered by topography upon encountering the meridional ridge. Over the ridge, conservation of potential vorticity results in strengthening of the horizontal shear and baroclinicity of the jet(s). At the crest of the ridge, both the eddy momentum and the eddy buoyancy fluxes are transiently upgradient. We hypothesize that the upgradient buoyancy fluxes, in particular, are a result of an abrupt transition in the orientation of the mean flow.

Immediately downstream of the ridge, the enhancement of barotropic shear becomes a source of EKE, but may

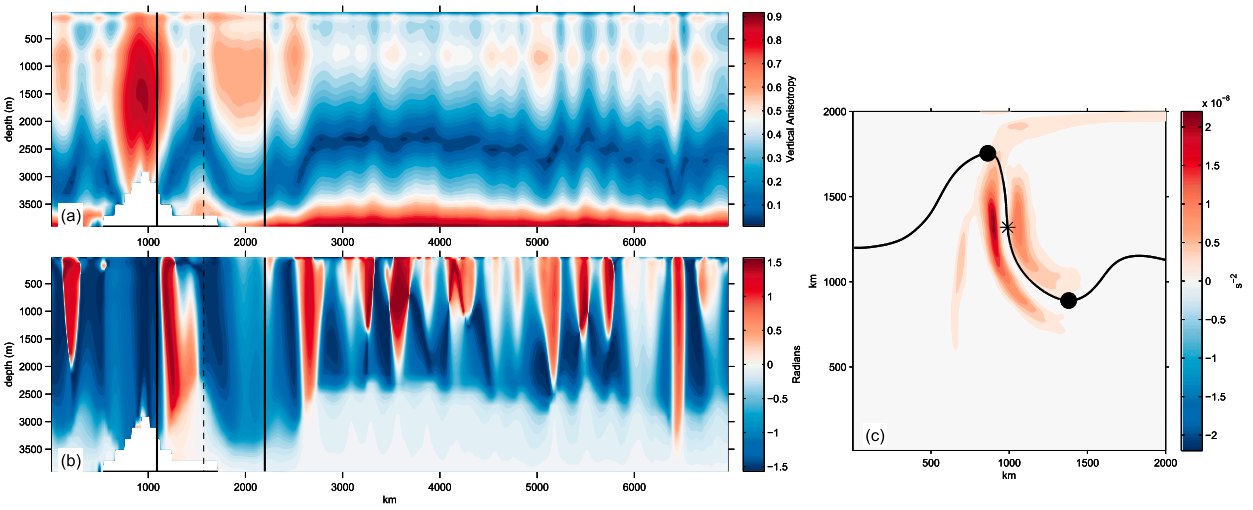

FIG. 9. As in Fig. 8, but for $\tau_0 = 0.2\,\mathrm{N\,m^{-2}}$ along the streamline shown in Fig. 7.

also act to suppress linear baroclinic instability through the distortion of normal modes. The displacement of the locations of maximum baroclinicity and maximum EKE has been linked to convective instability (Pierrehumbert 1984; Abernathey and Cessi 2014), which certainly contributes to the equilibrated distribution of EKE. However, the strongest release of EKE through baroclinic instability, diagnosed by D_{K_E}, is collocated with the release of EKE through barotropic instability, diagnosed by M_{K_E}, of a similar magnitude. This is indicative of the meander region being controlled by mixed barotropic–baroclinic instability.

Based on surface velocities retrieved from altimetric observations, restricting the analysis to barotropic eddy–mean flow interactions and to relatively coarse scales (~100 km), Williams et al. (2007) find that upstream of the maximum jet velocity the eddy vorticity fluxes are upgradient, while downstream of this region they are downgradient. This agrees well with the eddy momentum flux distributions seen in the barotropic component of our flow. The addition of a ridge also generates an alongstream evolution of the eddy–mean flow interactions that has a number of similarities to the idealized western boundary current jet studied by Waterman and Jayne (2011), for example, high horizontal eddy anisotropy on the flanks of the jet (Fig. 7). Abernathey and Cessi (2014) find that eddies generated in the meander are often advected downstream, where they continue to extract energy from the mean flow, which agrees with our understanding of the energy budget in our domain showing that some processes are nonlocal (Fig. 5). In agreement with our analysis of standing meanders, Bischoff and Thompson (2014) find that in the lee of topography isopycnal tilt increases due to the standing component of lateral buoyancy fluxes, but is relaxed due to the transient eddy buoyancy fluxes. Complementing these earlier studies, this analysis combines both baroclinic and barotropic instabilities and their impact on the mean flow, as summarized in Fig. 10.

6. Conclusions

This study provides one of the first applications of the geometric stability method, derived by Marshall et al.

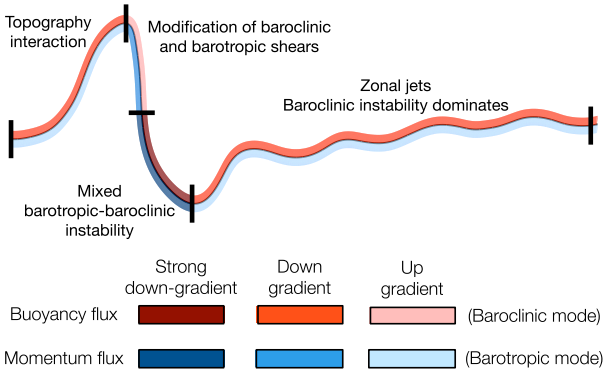

FIG. 10. Schematic summarizing the various regimes in the ACC-like channel; critically, there are multiple regimes within the meander region itself. Colors indicate the direction of the eddy buoyancy and momentum fluxes. Upstream of the meander as the flow encounters the topography, the convergence of streamlines both in the horizontal and vertical leads to an increase in eddy anisotropy. Immediately downstream of the ridge crest, the strong rotation of flow direction leads to upgradient buoyancy fluxes and upgradient and downgradient momentum fluxes. The flow becomes barotropically and baroclinically unstable, resulting in rapid generation of EKE. Downstream, zonal jets develop and baroclinic instability dominates with upgradient momentum fluxes.

(2012), to consider both barotropic and baroclinic components of the flow. The eddy–mean flow interactions implied from this analysis are consistent with energy conversion and regional Lorenz energy diagrams diagnosed in the simulations. The consideration of both barotropic and baroclinic instability characteristics reveals the importance of barotropic instability in the ACC.

The stability analysis of the ACC meander shows the detailed evolution of the flow's stability properties through the meander, which is summarized by Fig. 10. The region upstream of the meander is characterized by upgradient momentum fluxes and downgradient buoyancy fluxes, consistent with baroclinic instability and the barotropic governor. In the meander itself, we have both downgradient buoyancy and momentum fluxes consistent with both barotropic and baroclinic instability or mixed instability. Downstream of the meander, we have upgradient momentum fluxes and downgradient buoyancy fluxes, indicating continued baroclinic growth and barotropic decay.

Simulations run with two different wind stress magnitudes resulted in qualitatively similar patterns of eddy fluxes. However, as the forcing changed, the relative interactions between the baroclinic and barotropic flows were modified. This could modify tracer transport and impact the meridional overturning circulation. Accurately representing these fluxes is likely to be critical for simulating how energy is dissipated in numerical models of the Southern Ocean.

Acknowledgments. We are grateful for useful discussions with Andreas Klocker, David Marshall, Andrew Stewart, and Joe Pedlosky. The authors all acknowledge support from NSF OCE-1235488. MKY also acknowledges support from the AMS Graduate Student Fellowship.

REFERENCES

Abernathey, R., and P. Cessi, 2014: Topographic enhancement of eddy efficiency in baroclinic equilibration. *J. Phys. Oceanogr.*, **44**, 2107–2126, doi:10.1175/JPO-D-14-0014.1.

——, J. Marshall, and D. Ferreira, 2011: The dependence of Southern Ocean meridional overturning on wind stress. *J. Phys. Oceanogr.*, **41**, 2261–2278, doi:10.1175/JPO-D-11-023.1.

Bischoff, T., and A. F. Thompson, 2014: Configuration of a Southern Ocean storm track. *J. Phys. Oceanogr.*, **44**, 3072–3078, doi:10.1175/JPO-D-14-0062.1.

Bishop, S. P., P. R. Gent, and F. O. Bryan, A. F. Thompson, M. C. Long, and R. Abernathey, 2016: Southern Ocean overturning compensation in an eddy-resolving climate simulation. *J. Phys. Oceanogr.*, **46**, 1575–1592, doi:10.1175/JPO-D-15-0177.1.

Böning, C. W., A. Dispert, M. Visbeck, S. Rintoul, and F. U. Schwarzkopf, 2008: The response of the Antarctic Circumpolar Current to recent climate change. *Nat. Geosci.*, **1**, 864–869, doi:10.1038/ngeo362.

Chang, E. K. M., S. Lee, and K. L. Swanson, 2002: Storm track dynamics. *J. Climate*, **15**, 2163–2183, doi:10.1175/1520-0442(2002)015<02163:STD>2.0.CO;2.

Chapman, C. C., A. M. Hogg, A. E. Kiss, and S. R. Rintoul, 2015: The Dynamics of Southern Ocean storm tracks. *J. Phys. Oceanogr.*, **45**, 884–903, doi:10.1175/JPO-D-14-0075.1.

Chen, R., G. R. Flierl, and C. Wunsch, 2014: A description of local and nonlocal eddy–mean flow interaction in a global eddy-permitting state estimate. *J. Phys. Oceanogr.*, **44**, 2336–2352, doi:10.1175/JPO-D-14-0009.1.

——, A. F. Thompson, and G. R. Flierl, 2016: Time-dependent eddy-mean energy diagrams and their application to the ocean. *J. Phys. Oceanogr.*, **46**, 2827–2850, doi:10.1175/JPO-D-16-0012.1.

Downes, S. M., and A. M. Hogg, 2013: Southern Ocean circulation and eddy compensation in CMIP5 models. *J. Climate*, **26**, 7198–7220, doi:10.1175/JCLI-D-12-00504.1.

Dufour, C. O., and Coauthors, 2015: Role of mesoscale eddies in cross-frontal transport of heat and biogeochemical tracers in the Southern Ocean. *J. Phys. Oceanogr.*, **45**, 3057–3081, doi:10.1175/JPO-D-14-0240.1.

Ferrari, R., and M. Nikurashin, 2010: Suppression of eddy diffusivity across jets in the Southern Ocean. *J. Phys. Oceanogr.*, **40**, 1501–1519, doi:10.1175/2010JPO4278.1.

Hogg, A. M., M. P. Meredith, J. R. Blundell, and C. Wilson, 2008: Eddy heat flux in the Southern Ocean: Response to variable wind forcing. *J. Climate*, **21**, 608–620, doi:10.1175/2007JCLI1925.1.

——, ——, D. P. Chambers, E. P. Abrahamsen, C. W. Hughes, and A. K. Morrison, 2015: Recent trends in the Southern Ocean eddy field. *J. Geophys. Res. Oceans*, **120**, 257–267, doi:10.1002/2014JC010470.

Hoskins, B. J., and P. J. Valdes, 1990: On the existence of storm-tracks. *J. Atmos. Sci.*, **47**, 1854–1864, doi:10.1175/1520-0469(1990)047<1854:OTEOST>2.0.CO;2.

——, and K. I. Hodges, 2002: New perspectives on the Northern Hemisphere winter storm tracks. *J. Atmos. Sci.*, **59**, 1041–1061, doi:10.1175/1520-0469(2002)059<1041:NPOTNH>2.0.CO;2.

James, I., 1987: Suppression of baroclinic instability in horizontally sheared flows. *J. Atmos. Sci.*, **44**, 3710–3720, doi:10.1175/1520-0469(1987)044<3710:SOBIIH>2.0.CO;2.

——, and L. Gray, 1986: Concerning the effect of surface drag on the circulation of a baroclinic planetary atmosphere. *Quart. J. Roy. Meteor. Soc.*, **112**, 1231–1250, doi:10.1002/qj.49711247417.

Jones, C., and P. Cessi, 2016: Interbasin transport of the meridional overturning circulation. *J. Phys. Oceanogr.*, **46**, 1157–1169, doi:10.1175/JPO-D-15-0197.1.

Kaspi, Y., and T. Schneider, 2011: Downstream self-destruction of storm tracks. *J. Atmos. Sci.*, **68**, 2459–2464, doi:10.1175/JAS-D-10-05002.1.

——, and ——, 2013: The role of stationary eddies in shaping mid-latitude storm tracks. *J. Atmos. Sci.*, **70**, 2596–2613, doi:10.1175/JAS-D-12-082.1.

Killworth, P. D., 1980: Barotropic and baroclinic instability in rotating stratified fluids. *Dyn. Atmos. Oceans*, **4**, 143–184, doi:10.1016/0377-0265(80)90013-5.

Lu, J., and K. Speer, 2010: Topography, jets, and eddy mixing in the Southern Ocean. *J. Mar. Res.*, **68**, 479–502, doi:10.1357/002224010794657227.

Marshall, D. P., J. R. Maddison, and P. S. Berloff, 2012: A framework for parameterizing eddy potential vorticity fluxes. *J. Phys. Oceanogr.*, **42**, 539–557, doi:10.1175/JPO-D-11-048.1.

Marshall, G. J., 2003: Trends in the Southern Annular Mode from observations and reanalyses. *J. Climate*, **16**, 4134–4143, doi:10.1175/1520-0442(2003)016<4134:TITSAM>2.0.CO;2.

Marshall, J., and G. Shutts, 1981: A note on rotational and divergent eddy fluxes. *J. Phys. Oceanogr.*, **11**, 1677–1680, doi:10.1175/1520-0485(1981)011<1677:ANORAD>2.0.CO;2.

——, and K. Speer, 2012: Closure of the meridional overturning circulation through Southern Ocean upwelling. *Nat. Geosci.*, **5**, 171–180, doi:10.1038/ngeo1391.

——, A. Adcroft, C. Hill, L. Perelman, and C. Heisey, 1997: A finite-volume, incompressible Navier Stokes model for studies of the ocean on parallel computers. *J. Geophys. Res.*, **102**, 5753–5766, doi:10.1029/96JC02775.

Masich, J., T. K. Chereskin, and M. R. Mazloff, 2015: Topographic form stress in the Southern Ocean state estimate. *J. Geophys. Res. Oceans*, **120**, 7919–7933, doi:10.1002/2015JC011143.

Meredith, M. P., and A. M. Hogg, 2006: Circumpolar response of Southern Ocean eddy activity to a change in the Southern Annular Mode. *Geophys. Res. Lett.*, **33**, L16608, doi:10.1029/2006GL026499.

Nakamura, N., 1993: Momentum flux, flow symmetry, and the nonlinear barotropic governor. *J. Atmos. Sci.*, **50**, 2159–2179, doi:10.1175/1520-0469(1993)050<2159:MFFSAT>2.0.CO;2.

Naveira Garabato, A. C., R. Ferrari, and K. L. Polzin, 2011: Eddy stirring in the Southern Ocean. *J. Geophys. Res.*, **116**, C09019, doi:10.1029/2010JC006818.

Pedlosky, J., 1989: Simple models for local instabilities in zonally inhomogeneous flows. *J. Atmos. Sci.*, **46**, 1769–1778, doi:10.1175/1520-0469(1989)046<1769:SMFLII>2.0.CO;2.

——, 2013: *Geophysical Fluid Dynamics*. 2nd ed. Springer, 710 pp.

Pierrehumbert, R., 1984: Local and global baroclinic instability of zonally varying flow. *J. Atmos. Sci.*, **41**, 2141–2162, doi:10.1175/1520-0469(1984)041<2141:LAGBIO>2.0.CO;2.

Rivière, P., A. M. Treguier, and P. Klein, 2004: Effects of bottom friction on nonlinear equilibration of an oceanic baroclinic jet. *J. Phys. Oceanogr.*, **34**, 416–432, doi:10.1175/1520-0485(2004)034<0416:EOBFON>2.0.CO;2.

Solodoch, A., A. L. Stewart, and J. C. McWilliams, 2016: Baroclinic instability of axially symmetric flow over sloping bathymetry. *J. Fluid Mech.*, **799**, 265–296, doi:10.1017/jfm.2016.376.

Stewart, K., P. Spence, S. Waterman, J. Le Sommer, J.-M. Molines, J. Lilly, and M. England, 2015: Anisotropy of eddy variability in the global ocean. *Ocean Modell.*, **95**, 53–65, doi:10.1016/j.ocemod.2015.09.005.

Talley, L. D., 2011: *Descriptive Physical Oceanography: An Introduction*. 6th ed. Academic Press, 560 pp.

Tamarin, T., J. R. Maddison, E. Heifetz, and D. P. Marshall, 2016: A geometric interpretation of eddy Reynolds stresses in barotropic ocean jets. *J. Phys. Oceanogr.*, **46**, 2285–2307, doi:10.1175/JPO-D-15-0139.1.

Thompson, A. F., and K. J. Richards, 2011: Low frequency variability of Southern Ocean jets. *J. Geophys. Res.*, **116**, C09022, doi:10.1029/2010JC006749.

——, and J.-B. Sallée, 2012: Jets and topography: Jet transitions and the impact on transport in the Antarctic Circumpolar Current. *J. Phys. Oceanogr.*, **42**, 956–972, doi:10.1175/JPO-D-11-0135.1.

——, and A. C. Naveira Garabato, 2014: Equilibration of the Antarctic Circumpolar Current by standing meanders. *J. Phys. Oceanogr.*, **44**, 1811–1828, doi:10.1175/JPO-D-13-0163.1.

——, A. L. Stewart, and T. Bischoff, 2016: A multibasin residual-mean model for the global overturning circulation. *J. Phys. Oceanogr.*, **46**, 2583–2604, doi:10.1175/JPO-D-15-0204.1.

Vallis, G. K., 2006: *Atmospheric and Oceanic Fluid Dynamics: Fundamentals and Large-Scale Circulation*. Cambridge University Press, 745 pp.

Ward, M. L., and A. M. Hogg, 2011: Establishment of momentum balance by form stress in a wind-driven channel. *Ocean Modell.*, **40**, 133–146, doi:10.1016/j.ocemod.2011.08.004.

Waterman, S., and S. R. Jayne, 2011: Eddy-mean flow interactions in the along-stream development of a western boundary current jet: An idealized model study. *J. Phys. Oceanogr.*, **41**, 682–707, doi:10.1175/2010JPO4477.1.

——, and B. J. Hoskins, 2013: Eddy shape, orientation, propagation, and mean flow feedback in western boundary current jets. *J. Phys. Oceanogr.*, **43**, 1666–1690, doi:10.1175/JPO-D-12-0152.1.

——, and J. M. Lilly, 2015: Geometric decomposition of eddy feedbacks in barotropic systems. *J. Phys. Oceanogr.*, **45**, 1009–1024, doi:10.1175/JPO-D-14-0177.1.

Williams, P. D., P. L. Read, and T. W. Haine, 2010: Testing the limits of quasi-geostrophic theory: Application to observed laboratory flows outside the quasi-geostrophic regime. *J. Fluid Mech.*, **649**, 187–203, doi:10.1017/S0022112009993405.

Williams, R. G., C. Wilson, and C. W. Hughes, 2007: Ocean and atmosphere storm tracks: The role of eddy vorticity forcing. *J. Phys. Oceanogr.*, **37**, 2267–2289, doi:10.1175/JPO3120.1.